Jordan Journal of Physics

ARTICLE

Investigation Study on the Zn Doping Effect on the Structural and Morphological Characteristics of Fe_2O_3 Thin Films for Future Gas Sensor Applications

Jamal M. Rzaij,   Wisam D. Jalal   and   Ahmed M. Ahmed

Department of Physics, College of Science, University Of Anbar, Ramadi, Iraq.

Abstract: In this work, thin films of undoped hematite (α-Fe_2O_3) and Fe_2O_3 doped with various concentrations of Zn (2, 4, 6, and 8 at.%) were deposited on a glass substrate using the chemical spray pyrolysis technique. The effect of Zn ions on the structural, topographical, morphological, and chemical properties of hematite was investigated. Structural analysis revealed hematite phase crystallization with a hexagonal crystal structure, with crystallite sizes ranging from 36.7 to 50.2 nm. Topographical analysis showed surface features where atoms aggregated to form hill- and plateau-like structures, free of cracks. Grain sizes ranged from 43 to 80 nanometers. As the concentration of Zn dopant increased, there was an observed increase in both surface roughness and root-mean-square values. Morphological analysis indicated a porous microstructure with surface porosity increasing as Zn concentration rose. The average particle size increased from 86 to 114 nm at a Zn concentration of 8 at.%. Therefore, it can be concluded that the hematite doped with Zn^{2+} exhibits promising characteristics for utilization in gas sensor devices.

Keywords: Thin film, Fe_2O_3, Zinc concentration, Doping effect, Structural, AFM, Spray pyrolysis.

PACs: 87.15.-v, 68.47.Pe.

Introduction

Nanocrystalline oxides have recently gained significant attention of researchers due to their high surface area-to-volume ratio, which enhances their ability to absorb a significant amount of radiation falling on the material and convert it into electric current, as in solar cells [1], or to adsorb oxygen atoms on the film surface and affect the electrical conductivity, as in gas sensor devices [2]. Hematite ferric oxide (α-Fe_2O_3) is one such semiconductor oxide, known for its low toxicity, biocompatibility, structural stability, and soft ferromagnetic properties at ambient temperatures [3, 4]. As a result, α-Fe_2O_3 applications in photocatalysts [5], solar cells [6], lithium-ion batteries [7], and gas sensors [8] have been widely investigated.

Several methods are used today to modify materials for their intended purposes [9]. These methods include ion doping, shape control, heterostructure construction, and catalyst addition. Ion doping and shape control are useful and effective methods to improve the physical and chemical characteristics of semiconductor oxide thin films [10]. Ti doping effect on Fe_2O_3 photoactive electrodes was presented by Zandi *et al.* [11]. They have found that the Ti dopant atoms improve the photoelectric properties of the Fe_2O_3 thin film in a study on the Ti doping role on the Fe_2O_3 photoelectrochemical performance. The sensing capability of the Zn-doped microcubes of Fe_2O_3 which were produced via the hydrothermal method was characterized by

Song *et al.* [12]. The results of the study indicate that the use of Zn makes it possible to adjust the Debye length of the fabricated sensor, increasing the sensitivity of the Fe_2O_3 thin film sensor. The hydrothermal synthesis of Sn-doped hematite nanoparticles was discussed by Lam *et al.* [13]. Their study outcomes revealed that the Sn-doped Fe_2O_3 has the imminent capability of effectively participating in the photocatalytic degradation of inorganic dyes, such as those found in wastewater.

Fe_2O_3 is an example of few semiconductors with a precise valence band position for the evolution or dissociation of oxygen, making it a promising catalytic material. However, due to the rapid recombination of charge carriers, the catalytic activity of α-Fe_2O_3 remains much lower, reducing its effectiveness in optoelectronic and sensing devices [5]. Numerous methodologies have been developed to address this challenge. One feasible approach involves doping α-Fe_2O_3 with additional metal ions as a way of reducing this limitation. Doping with metals like zinc (Zn), titanium (Ti), chromium (Cr), aluminum (Al), nickel (Ni), and cobalt (Co) at the Fe site influences hematite's physical and catalytic properties [14].

The impact of zinc cation on hematite's structural, electrical, and optical characteristics is emerging as a topic of scientific interest. Substituting Fe^{3+} with Zn^{2+} induces an electrical charge disparity within the crystal structure (hematite host lattice). To preserve charge neutrality, this substitution may trigger one or more mechanisms: conversion of Fe^{3+} to Fe^{2+}, generation of cation vacancies, and subsequent occupation of oxygen vacancies. According to a study conducted by Velev *et al.* [15], Zn^{2+} influences the electronic properties of hematite by producing a hole in the valence band of oxygen. The additional hole produced from the zinc ion with a charge of 2+ is positioned on the neighboring oxygen sites, thereby creating an acceptor level that is located below the Fermi energy level. The delocalization of this hole makes it a promising candidate for exhibiting high conductivity. Incorporating Zn 2+ ions facilitates the electron hopping mechanism through Fe^{3+}–Fe^{2+} pairs while altering the physical characteristics of α-Fe_2O_3. Moreover, zinc cation (Zn^{2+}) investigation has been frequently addressed due to its potential to enhance the carrier lifetime and expand the absorption range of hematite Fe_2O_3 catalysts by conducting Zn-doping [16].

Based on these principles, this study synthesizes undoped and Zn-doped Fe_2O_3 thin films via chemical spray pyrolysis to investigate the effects of varying Zn concentrations on the structural, topographical, morphological, and elemental properties of Fe_2O_3 thin films. Structural properties were analyzed using X-ray diffraction (XRD), surface topography was examined with atomic force microscopy (AFM), surface morphology was studied with scanning electron microscopy (SEM), and elemental composition was assessed with energy-dispersive X-ray spectroscopy (EDX).

Experimental Work and Procedure

Precursor solutions of undoped ferric oxide (Fe_2O_3) and Fe_2O_3 doped with various Zn concentration ratios (2, 4, 6, and 8 at.%) were prepared separately and deposited on glass substrates using the low-cost technique of chemical spray pyrolysis. All powders used in the study were purchased from BDH Chemical Ltd., Poole, England, with a purity of 99%.

A 0.01 molar iron chloride solution was prepared by dissolving 0.198 g of iron chloride dihydrate ($FeCl_3.2H_2O$) in 100 ml of distilled water. As a source of zinc ions, a 0.01 M zinc chloride solution was synthesized by dissolving 0.086 g of zinc chloride dihydrate ($ZnCl_2.2H_2O$) in 50 ml of distilled water. The ferric precursor solution was doped with the zinc precursor solution at different concentrations, and then the obtained solutions were mixed using the ultrasonic bath for 15 minutes at 30°C.

Glass substrates were cleaned using distilled water and ethanol before the prepared solutions were deposited under a set of controlled conditions: a deposition temperature of 350 °C, a spray time of 10 seconds, a stop time of 25 seconds, a distance of 3 ± 28 cm between the substrate and the atomizer nozzle, and a gas carrier (oxygen) pressure of 3 millibars with 2 ml per minute flow rate. The prepared films were then annealed for one hour at 450°C in air. Scanning electron microscopy images and ImageJ software were used to determine the thickness of the deposited films, which were measured as 180, 205, 228, 239, and 254 nm for the undoped and Fe_2O_3 films doped with 2, 4, 6, and 8 at.% Zn, respectively.

Result and Discussion

Structural Properties

The X-ray diffraction pattern of undoped and Fe$_2$O$_3$ doped with varying Zn concentrations thin films (Fe$_2$O$_3$:Zn) are shown in Fig. 1. The results demonstrate that the deposited Fe$_2$O$_3$ films are polycrystalline and indexed to hexagonal phase. The diffraction peaks at (104), (110), (113), (024), (116), (018), and (214) correspond to diffraction angles (2-theta) of 33.161º, 35.627º, 40.86º, 49.461º, 54.072º, 57.608º, and 62.432º,

respectively, in accordance with the reference JCPDS 96-900-0140.

Additionally, it was shown that the (104) diffraction peak is the sharpest, indicating the dominating directionality of crystal growth, in agreement with the findings in the literature [17, 18]. The absence of diffraction peaks aside from those associated with hematite indicates that Zn atoms have been incorporated into the α-Fe$_2$O$_3$ matrix. Consequently, the presence of dopant atoms affects the crystallinity without altering the hexagonal structure of hematite.
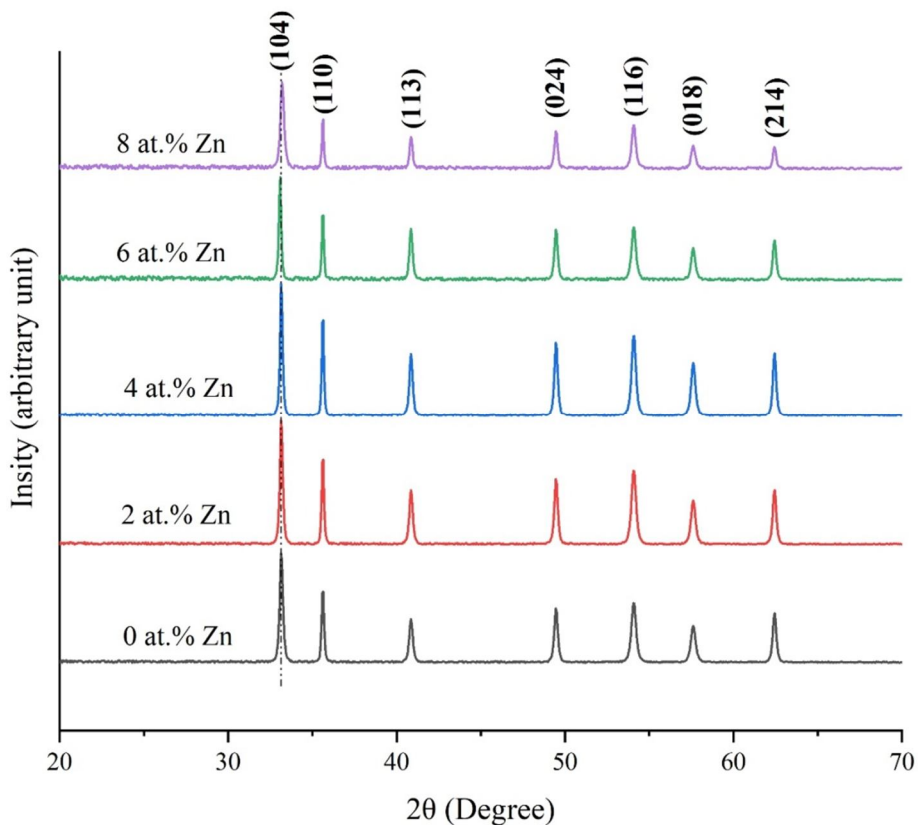

FIG. 1. XRD spectra of undoped Fe$_2$O$_3$ and Fe$_2$O$_3$ doped with 2, 4, 6, and 8 at.% Zn.

Figure 2 depicts the Rietveld refinement of the X-ray diffraction data, utilizing the full-pattern fitting method, for both undoped and Fe$_2$O$_3$ doped with 8 at.% Zn. The Rietveld refinement method is utilized to conduct a quantitative analysis of the Fe$_2$O$_3$ crystalline phase compared to the amorphous phases of the Fe$_2$O$_3$ structure or additional minor phases. The findings obtained from Rietveld refinement

reveal that the X-ray diffraction pattern of the as-deposited Fe$_2$O$_3$ film, as depicted in Fig. 2(a), exhibits a high degree of conformity with the diffraction data of the standard lines. However, the degree of conformity is reduced for the sample doped with 8 at.% Zn, as illustrated in Fig. 2(b). This suggests that the doping process successfully altered the structural characteristics of the Fe$_2$O$_3$ film [19].
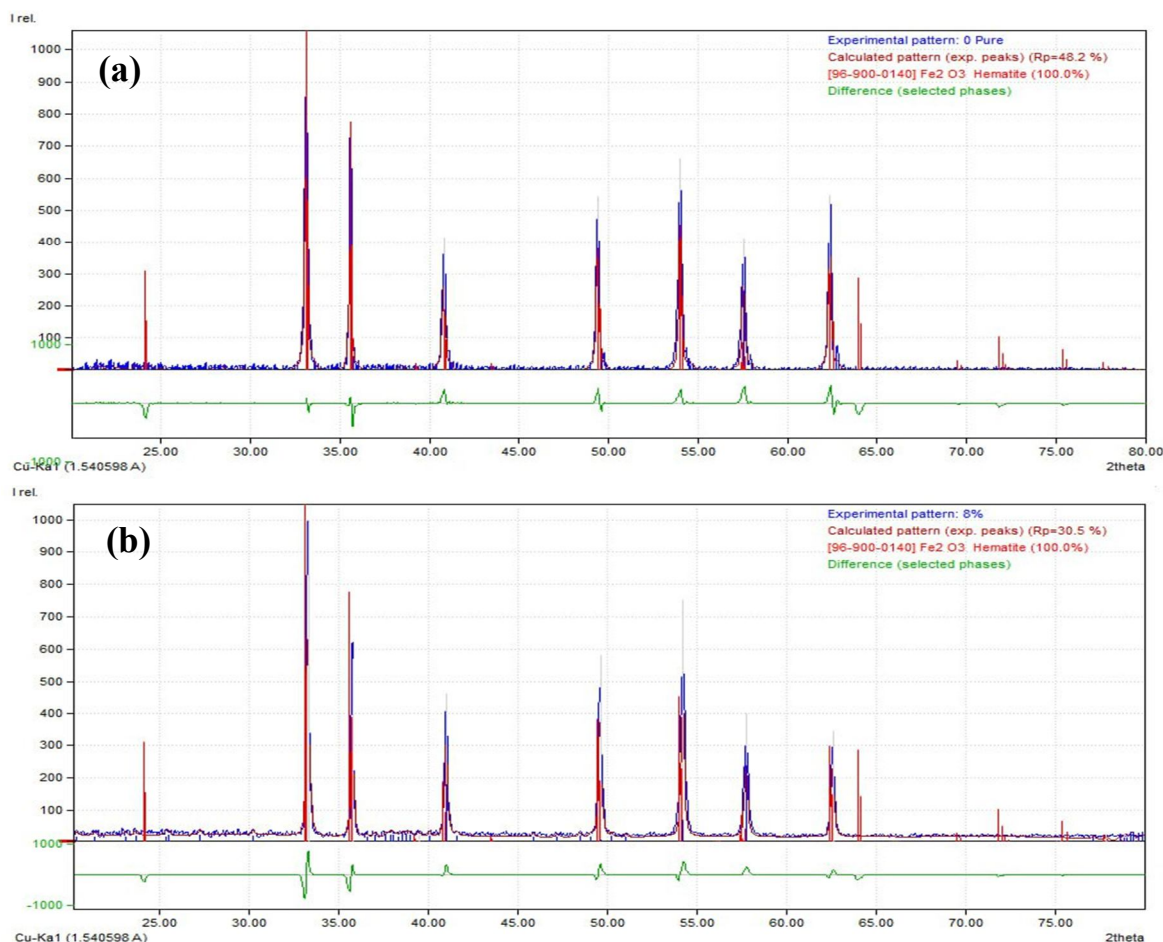
FIG. 2. Rietveld refinement of the XRD patterns of (a) as-deposited Fe_2O_3 and (b) 8 at.% Zn-doped Fe_2O_3.

XRD analysis indicates that the (104) diffraction peak experiences a shift towards the lower diffraction when Zn doping increases to 6 at.%, followed by a shift towards the higher diffraction angle at a Zn concentration of at. 8 %. The shift of XRD peaks results in variations in the lattice parameters (a and c) in addition to the unit cell volume (V), as presented in Table 1. This investigation suggests that at lower Zn doping levels (below 4 at.%), Zn atoms primarily occupy substitutional sites [20]. In comparison, higher doping concentrations of Zn occupy partial interstitial sites or segregate on the surface, distorting the host lattice structure. The incorporation of Zn^{2+} ions, which are larger than Fe^{3+} ions, into the host lattice is expected to result in distortion, resulting in stress within the system [21]. The stress (σ) is calculated by using Eq. (1) [21], with results listed in Table 1. The negative stress values obtained suggest the presence of compressive stress within the system [22].

$$\sigma = \frac{c - c_\circ}{c_\circ}, \tag{1}$$

where c and $c_\circ$ are, respectively, the lattice constant from the JCPDS standard card and the results of XRD.

TABLE 1. The structural parameters of undoped Fe_2O_3 and Zn-doped Fe_2O_3 thin films.

Samples	D (nm)	Lattice constant (Å)		$\sigma \times 10^{10}$ dynes/cm^2	$\delta \times 10^{-4}$ (lines/nm^2)	V (Å^3)
		a	c			
0 at.% Zn	36.7	5.035	13.731	-11.63	74.24	301.45
2 at.% Zn	40.5	5.039	13.733	-10.18	60.96	301.97
4 at.% Zn	46.1	5.042	13.736	-8.001	47.05	302.40
6 at.% Zn	50.2	5.051	13.739	-5.81	39.68	303.54
8 at.% Zn	31.8	5.003	13.711	-26.18	98.88	297.19

Depending on the dominant diffraction peak (104), the crystallite size (D) was calculated using Scherrer's formula, Eq. (2). The findings indicate a correlation between the concentration of Zn dopant and the crystallite size: as Zn concentration increases up to 6 at.%, the crystallite size increases, then decreases when the Zn dopant concentration increases to 8 at.%, as demonstrated in Table 1.

$$D = \frac{k\lambda}{\beta \cos\theta},\qquad(2)$$

where $k \approx 0.9$ is the shape factor, $\lambda = 1.54060$ Å is the Cu kα radiation wavelength, β (measured in radians) is the full width at half maximum (FWHM) of the diffraction peak, and θ is Bragg's angle of the diffraction. The increase in crystallite size corresponds to the inclusion of Zn, which is a significant factor in the growth of crystals and Fe$_2$O$_3$ crystallization. The increase in crystallite size can be attributed to replacing Fe^{3+} ions with Zn^{2+} ions, which are comparatively larger. Thu trend observed in the crystallite size of Fe$_2$O$_3$ samples with higher Zn doping is consistent with the findings reported in earlier studies on ZnO doped with Y, CeO$_2$ doped with Mn, and ZnO doped with Mg [23–25]. Moreover, the evaluation of the dislocation density (δ) which is derived as ($\delta = 1/D^2$) offers additional insights into the defects in the prepared samples. The dislocation density for the 6 at.% Zn sample was relatively low, which indicates a high quantity of defects that can be used to improve the sensor sensitivity. However, the defects tend to be decreased at the doped sample of at. 8% Zn, as shown in Table 1. This suggests that, up to 6 at.% Zn, dopant atoms are well-integrated into the lattice, increasing crystallite size and reducing dislocation density. With a doping concentration of around 8 at.% of Zn, the size of the crystallites decreases as the number of dislocations density increases. This indicates that the dopant atoms pour into the interstitial lattice sites, making the crystal arrangement less regular and the dislocation density higher [26]. Through the changes in dislocation density and stress seen in the prepared samples, it could be inferred that the

materials contain lattice structure defects, which impact the mechanical properties of the synthesized thin films. As crystallite size is crucial for the interaction of metal oxide thin films with gas molecules, optimizing crystallite structure and size can improve sensor response to target gases [27].

Atomic Force Microscopy (AFM)

The surface topography of the deposited thin films was analyzed using AFM to determine the topography of the films' surfaces, average grain size (Gs), average roughness (Ra), and root-mean-square roughness (Rs). Figure 3 displays 3D AFM images of Fe$_2$O$_3$ and Zn-doped Fe$_2$O$_3$ at various Zn concentrations. The AFM images reveal that the atoms are spread without cracks along the surface of the films, aggregating into a hill-and-plateau-like structure. The height of the hills grows as doping with zinc increases, which contributes to an increase in surface roughness rate [28]. High-roughness surfaces contribute to enhanced sensor performance by increasing surface area, increasing atom diffusion, and thereby creating more potential sites for surface reactions and oxygen molecule adsorption [29]. Table 2 confirms that the surface topography of Fe$_2$O$_3$ is strongly affected by Zn doping, which increases the Gs and Ra as the Zn at.% increases. The aggregation of smaller grains into larger grains is enhanced by increasing film thickness, increasing grain size, and, consequently, surface roughness [30]. Furthermore, the rise in root-mean-square roughness indicates that the grain growth on the glass substrates occurred perpendicular to the film's surface during the deposition process [31]. This is supported by the notable color variation observed in the 3D AFM images, which indicates that the deposited atoms exhibit variations in growth regarding their vertical positioning. Increases in particle size contribute to increased sensor response by increasing the area exposed to gas molecules, increasing the rate of interaction between the surface of the sensor film and the molecules of the target gas [32].
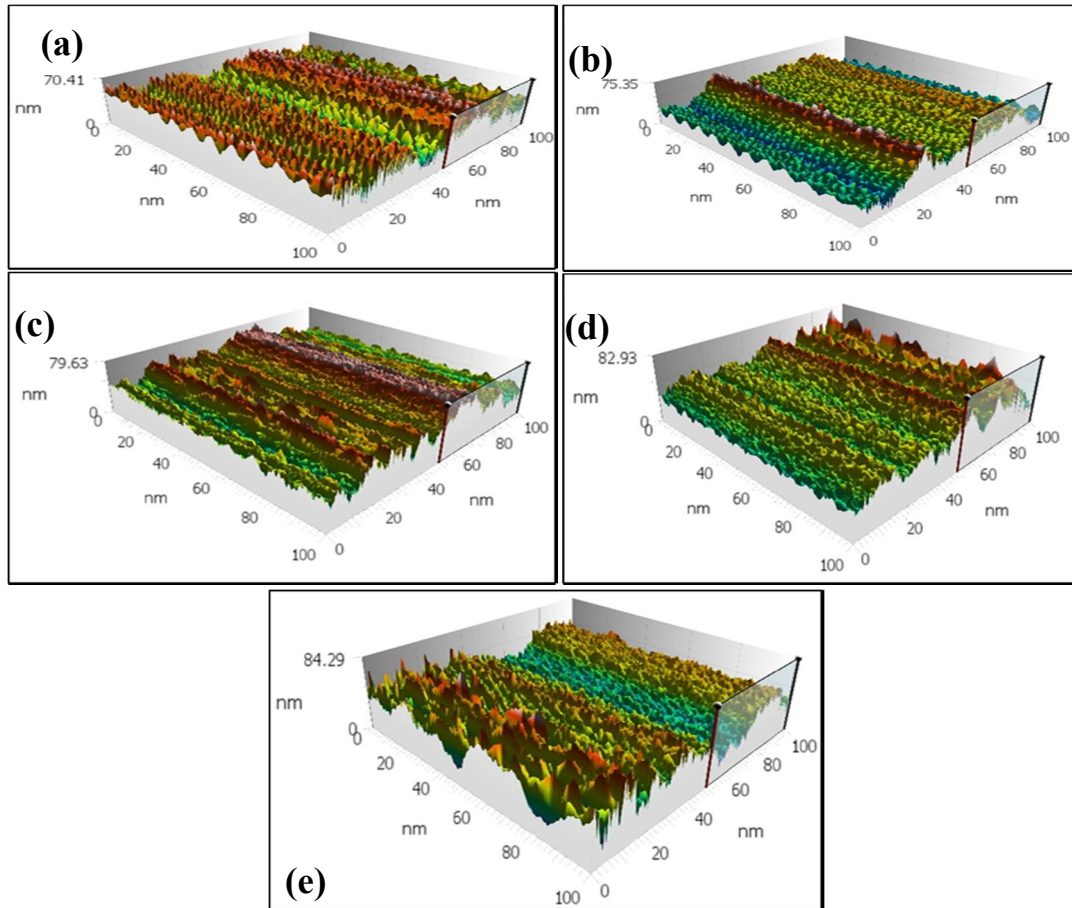
FIG. 3. AFM images of (a) Fe_2O_3 and Zn-doped Fe_2O_3: (b) 2 at.% Zn, (c) 4 at.% Zn, (d) 6 at.% Zn, and (e) 8 at.% Zn thin films.

TABLE 2. AFM Parameters of Fe_2O_3:Zn thin films.

Samples	Gs (nm)	Ra (nm)	Rs (nm)
0 at.% Zn	43	70.41	9.77
2 at.% Zn	48	75.35	10.92
4 at.% Zn	60	79.63	11.05
6 at.% Zn	67	82.93	12.06
8 at.% Zn	80	84.29	12.27

Morphological Analysis

SEM micrographs of undoped Fe_2O_3 and doped with various Zn concentrations are shown in Figs. 4 (a)-4(e). The microstructure of the film doped with 8 at.% Zn exhibits a significantly porous surface. It can be concluded that the porosity of films increases as the concentration of Zn doping increases. The high porosity of the film surface in gas sensor applications provides more accessibility to the bulk of the film, increasing the active area for gas adsorption on the film surface [27]. The average particle size of the samples was estimated using ImageJ software. According to the findings, the as-deposited Fe_2O_3 film exhibits an average particle size of 43 nm. However, the samples doped with varying concentrations of Zn, namely 2 at.%, 4 at.%, 6 at.%, and 8 at.%, exhibit average particle sizes of 68, 81, 97, and 114 nm, respectively. The doped film of 8 at.% Zn exhibits larger grains, contributing to its high porosity nature [33] and consequent increase in the average roughness. This observation is consistent with the results obtained from the AFM analysis. The findings indicate that zinc doping plays a crucial role in shaping the surface morphology of the deposited films.
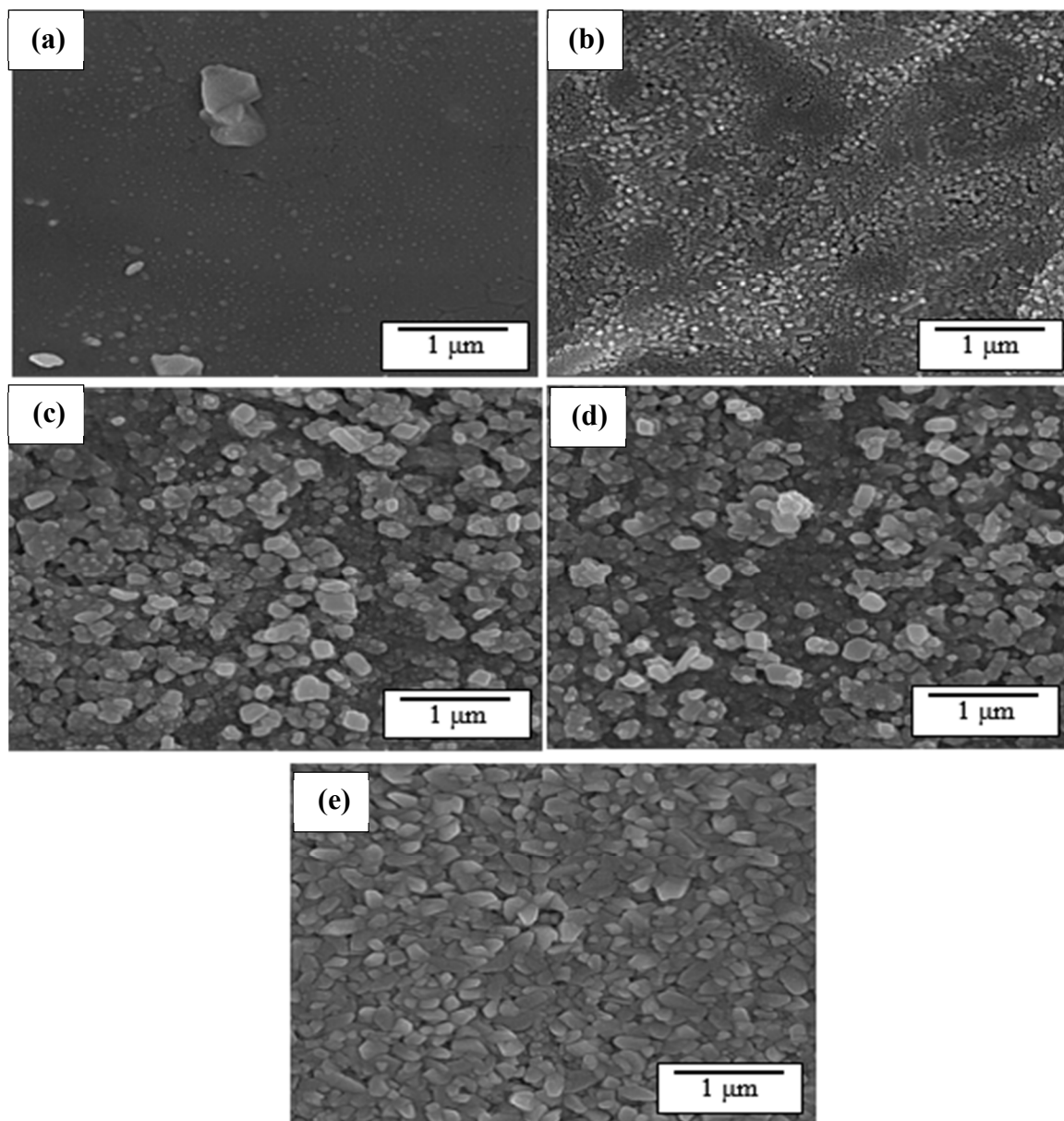
FIG. 4. SEM micrograph images of (a) as-deposited Fe$_2$O$_3$ and (b)-(e) Fe$_2$O$_3$:Zn thin films.

Energy Dispersive X-ray Spectroscopy (EDX)

Energy dispersive X-ray spectroscopy (EDX) measurements were conducted to verify the existence of Zn within the synthesized Fe$_2$O$_3$ thin film. Table 3 presents the elemental analysis results for Fe$_2$O$_3$:Zn nanostructured thin films, while Fig. 5 displays the EDX spectrum of Fe$_2$O$_3$ with 8 at.% Zn doping.

TABLE 3. EDX data of Zn-doped Fe$_2$O$_3$ thin films at various Zn at.%.

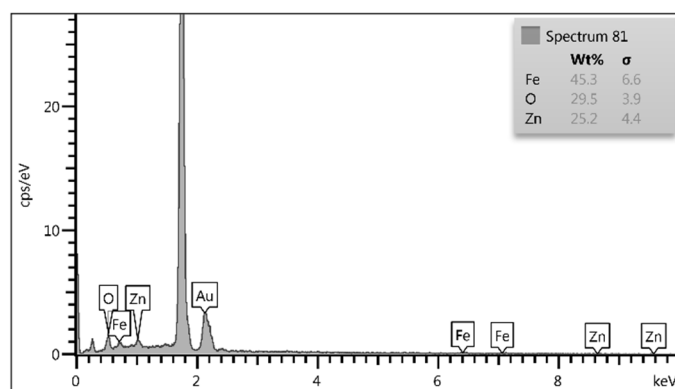| Samples	Percentage of the elements% (Wt%)			
	Fe	O	Zn	Zn/Fe ratio
0 at.% Zn	68.4	29.4	2.2	0.032
2 at.% Zn	65.5	27.7	5.8	0.089
4 at.% Zn	51.6	33.3	15.1	0.293
6 at.% Zn	57.8	26.0	22.07	0.382
8 at.% Zn	45.3	29.5	25.2	0.556

FIG. 5: EDX spectrum of Fe_2O_3 doped with 8 at.% Zn thin film.

The EDX spectrum indicates the absence of additional elements in the deposited thin films, except for the gold element. This finding verifies the high purity of the samples and the successful incorporation of zinc ions into the Fe crystal lattice. The gold coating used on non-conductive substrates for typical SEM applications may be responsible for the Au peak in the EDX spectrum. As shown in Table 3, increasing Zn concentrations corresponded to a decrease in the weight percentage of Fe and an increase in the weight percentage of Zn. This pattern further confirms the successful incorporation of Zn ions into the Fe matrix.

Conclusion

In summary, thin films of undoped Fe_2O_3 and Fe_2O_3 doped with different concentrations of Zn were developed on glass substrates by chemical spray pyrolysis. The synthesized films were characterized using XRD, AFM, SEM, and EDX to investigate the effects of Zn dopant on various Fe_2O_3 characteristics. XRD analysis confirmed that all the films showed a nanocrystalline hematite phase. Variations in diffraction peak intensity and crystallite size demonstrated the influence of zinc ions on the structural properties of the Fe_2O_3 film. AFM analysis showed that zinc doping increased film thickness, grain size, and surface roughness. SEM micrographs indicated that the porosity of the films exhibited an enhancement as the Zn doping concentration increased, with the film doped with 8 at.% Zn exhibiting the highest degree of porosity, providing an active surface area conducive to gas sensing applications. The findings suggest that the most optimal conditions for fabricating Fe2O3 thin films as sensor devices are achieved with 8 at.% Zn doping.

Conflict of Interest

The authors declare that they have no known competing financial interests or personal relationships that could have influenced the work reported in this paper.

References

[1] Fang, S., Chen, B., Gu, B., Meng, L., Lu, H., and Li, C.M., Mater. Adv., 11 (2) (2021) 3629.

[2] Hanfoosh, S.M. and Hassan, N.K., Iraqi J. Sci., 9 (60) (2019) 2009.

[3] Al-Haj, M. M., Jordan J. Phys., 2 (12) (2019) 133.

[4] Al-Hwaitat, E.S., Dmour, M.K., Bsoul, I., Albgour, A., Alsalti, T., Abuawad, R., Alajarmah, A., Al-Buqain, R., and Mahmood, S. H., Jordan J. Phys., 4 (14) (2021) 287.

[5] Suman, S.C., Kumar, A., and Kumar, P., Crystals, 4 (10) (2020) 273.

[6] Bouhjar, F., Mollar, M., Ullah, S., Marí, B., and Bessaïs, B., J. Electrochem. Soc., 2 (165) (2018) H30.

[7] Zhang, C., Chen, Z., Wang, H., Nie, Y., and Yan, J., ACS Appl. Nano Mater., 9 (4) (2021) 8744.

[8] Qin, Q., Olimov, D., and Yin, L., Chemosensors, 7 (10) (2022) 267.

[9] Mohsen, A. and Rzaij, J. M., J. Chem. Rev., 3 (2) (2020) 148.

[10] Chen, J., Xu, L., Li, W., and Gou, X., Adv. Mater., 5 (17) (2005) 582.

[11] Zandi, O., Klahr, B. M., and Hamann, T. W., Energy Environ. Sci., 2 (6) (2013) 634.

[12] Song, H., Sun, Y., and Jia, X., Ceram. Int., 10 (41) (2015) 13224.

[13] Lam, V.N., Vu, T.B., Do, Q.D., Le, T.T.X., Nguyen, T.D., Nguyen, T.-T.-B., Do, H.T., and Nguyen, T.T.O., J. Semicond., 12 (43) (2022) 122001.

[14] Wang, G., Ling, Y., Wheeler, D.A., George, K.E.N., Horsley, K., Heske, C., Zhang, J.Z., and Li, Y., Nano Lett., 8 (11) (2011) 3503.

[15] Velev, J., Bandyopadhyay, A., Butler, W.H., and Sarker, S., Phys. Rev. B, 20 (71) (2005) 205208.

[16] Lassoued, A., J. Mol. Struct., 1239 (2021) 130489.

[17] Mansour, S.A. and Ibrahim, M.M., J. Electron. Mater., 11 (46) (2017) 6502.

[18] Suresh, R., Giribabu, K., Manigandan, R., Stephen, A., and Narayanan, V., RSC Adv., 33 (4) (2014) 17146.

[19] Ibrahim, I.M., Rzaij, J.M., and Ramizy, A., Dig. J. Nanomater. Biostructures, 4 (12) (2017) 1187.

[20] Ibraheam, A.S., Rzaij, J.M., and Arshad, M. K. M., J. Electron. Mater., 1 (52) (2023) 414.

[21] Vijayalakshmi, K., Renitta, A., and Karthick, K., Ceram. Int., 4 (40) (2014) 6171.

[22] Rzaij, J. M., Sensors Actuators A Phys., 363 (2023) 114748.

[23] Kumar, P., Singh, V., Sharma, V., Rana, G., Malik, H.K., and Asokan, K., Ceram. Int., 5 (41) (2015) 6734.

[24] Kumar, P., Kumar, P., Kumar, A., Meena, R.C., Tomar, R., Chand, F., and Asokan, K., J. Alloys Compd., 672 (2016) 543.

[25] Kumar, P., Singh, J.P., Malik, H.K., Gautam, S., Chae, K.H., and Asokan, K., Superlattices Microstruct., 78 (2015) 183.

[26] Rzaij, J.M., Ibraheam, A.S., and Abass, A.M., Baghdad Sci. J., 2 (18) (2021) 401.

[27] Marei, J.M., Khalefa, A.A., Abduljabbar, Q.A., and Rzaij, J.M., J. Nano Res., 70 (2021) 41.

[28] Abduljabbar, Q.A., Radwan, H.A., Marei, J.M., and Rzaij, J.M., Eng. Res. Express, 1 (4) (2022) 015028.

[29] Liu, H., Shen, W., Chen, X., and Corriou, J.-P., J. Mater. Sci. Mater. Electron., 21 (29) (2018) 18380.

[30] Rzaij, J.M. and Habubi, N.F., J. Mater. Sci. Mater. Electron., 15 (33) (2022) 11851.

[31] Ma, X., Zhao, J., Du, W., Zhang, X., and Jiang, Z., J. Mater. Res. Technol., 3 (8) (2019) 3175.

[32] Jebur, K.H., J. Pet. Res. Stud., 1 (12) (2022) 226.

[33] Payton, R.L., Chiarella, D., and Kingdon, A., Sci. Rep., 1 (12) (2022) 7531.